ISSN 1063-7745, Crystallography Reports, 2020, Vol. 65, No. 6, pp. 968–979. © Pleiades Publishing, Inc., 2020.

PHYSICAL PROPERTIES OF CRYSTALS

Enhanced Optical Properties of FeS_2 Using Ni@Cu Doping and Characterization of the Structural and Chemical Compositions for Solar Cell Applications

M. Riju Khandaker[a], M. Kamruzzaman[b,*], R. Afrose[b], M. Rahman[c], M. K. R. Khan[a], M. N. H. Liton[b], M. A. Helal[b], T. K. Anam[b], and M. M. Rahman[a]

[a] *Department of Physics, University of Rajshahi, Rajshahi, 6205 Bangladesh*

[b] *Department of Physics, Begum Rokeya University, Rangpur, Rangpur, 5400 Bangladesh*

[c] *Department of Textile Engineering, Uttara University, Dhaka, 1230 Bangladesh*

**e-mail: kzaman.phy11@gmail.com*

Received July 3, 2020; revised July 3, 2020; accepted July 6, 2020

Abstract—Transition metals doped FeS_2 thin films are promising materials for optoelectronics, energy saving and storage applications. This is a first time report on the simultaneously Ni@Cu doped $Fe_{1-x}M_xS_2$ (M = Ni@Cu = 0, 2, 5, 10, and 20 at %) thin films fabricated by a simple chemical spray pyrolysis technique. In this paper we investigate the impact of doping on the structural, chemical states, optical properties and band gap nature by different characterization techniques. The SEM results show that surface morphology and granular grain size changes with the increment of Ni@Cu content which are coherent with the XRD results. The EDX and XPS measurements exhibit that the films are composed of Fe, S, Ni, and Cu elements whilst the films were slightly oxidized due to processing in the atmospheric conditions. Spectroscopy ellipsometry (SE) analysis demonstrates that the indirect band gap gradually increased from 1.38 eV (FeS_2) to 1.64 eV (Ni@Cu = 10 at %) while at higher doping the band gap was decreased to 1.53 could be due to incomplete doping. So, the band gap of FeS_2 can be tuned in between 1.38 and 1.64 eV by simultaneous Ni@Cu doping could be a suitable candidate for absorber application in solar cell devices. The other optical constants (dielectric constants, refractive index and extinction coefficient) explicitly carried out using SE measurement. Interestingly, progressing the absorption nature and bang gap in the visible region disclose a significant impact on the optical properties for optoelectronics applications.

DOI: 10.1134/S1063774520060188

INTRODUCTION

Renewable energy basically solar energy utilization is an essential alternative to fossil fuels. Solar energy is an excellent candidate for mitigating energy demand crisis due to its advantages of abundance and non-polluting nature. Solar energy can be converted into electricity by photovoltaic effect through a device produced by electrons–holes pair generation. The present photovoltaic market is dominated by c-Si based solar cells which exhibited power conversion efficiency (PCE) of 8–25% [1], but the PCE of the commercial products are in the range of 15–18% due to low absorption coefficient and significant heat loss produce in indirect band gap Si [2]. While they are fragile, very expensive and manufacturing processes is complex. Hence they may take several years to gain the payback which are the limiting for next generations applications. Thus researchers are exploring alternative to Si-absorbing materials having high extinction coefficients, band gap commensurate with the solar photon flux, earth abundance, low cost and non-toxic, etc. It is because a lot of research works have been intensively and extensively performed on the emerging light harvesting semiconductors thin films materials. For example, organohalide lead(II), perovskites group methylammonium lead(II), iodide ($CH_3NH_3PbI_3$) [3], copper indium gallium selenide (CIGS) [4], copper zinc tin sulfide (CZTS) [5], quantum dot sensitised CdTe, CdS, PbS, CdSe [6–13] and the chalcogenides group: $CuGaSe_2$, $CuInS_2$, $CuInSe_2$, Sb_2S_3, Sb_2Se_3, $CuGaS_2$ [8, 10, 14, 15] are excellent solar harvesters and highly efficient counter electrodes for promising use in inorganic, organic dye/quantum dot sensitized solar cells [16]. However, these materials suffer from potential barriers to mass production for commercialization due to their toxicity, scarcity of constituent elements (one or more of elements), expensiveness, or stability to humidity issues. On the other hand, non-toxic, earth abundance transition metal disulfides with a formula of MS_2 (M = Fe, Ni,

Ti, etc.) have been attracted extremely due to possessing intriguing physical, electrical, optical and magnetic properties. Among them, iron pyrite (FeS_2) has been widely studied because of high absorption coefficient (>10^5 cm^{-1}) at photon energy $hv > 1.3$ eV which is almost two orders of magnitude larger than c-Si [17–19], minority carrier diffusion length (100–1000 nm), high extinction coefficients, earth abundance, robust, biocompatible elements, non-toxicity. FeS_2 is an indirect band gap semiconductor shown theoretically with a band gap of 0.95–1.18 eV [20–22] and experimentally 0.95 eV, while the direct band gap of 1.03 eV [20, 23, 24]. The value of the band gap commensurate with the solar photon flux and its cost performance is good. The FeS_2 based photovoltaic cells exhibit power conversion efficiency of ~3% and low open circuit photovoltages attributed due to surface defects [25]. But the devices demonstrated high quantum efficiencies (>90%) and large photocurrents (>40 mA cm^{-2}) [25].

So, enhancing the photovoltage and efficiency of pyrite based solar cells require basic research on the growth, surface passivation, structural and electronic characterization of pyrite films [25]. To this point of view, many strategies have been employed in experimental and theoretical studies [15–33] such as, band gap tuning by doping/alloying [34–37] and/by making pyrite composites [36–38]. Many approaches have been employed for preparing undoped and doped FeS_2 thin films such as electrochemical deposition [39], spray pyrolysis [40], sulfurization of iron films, successive ionic layer adsorption and reaction (SILAR) method [41, 42], ion beam sputtering [43], thermal evaporation [44], metal-organic chemical vapor deposition [45], chemical vapor deposition (CVD) [46, 47] and molecular beam epitaxy (MBE) [48]. Among these approaches, the versatile spray pyrolysis technique is a cost-effective, easy to scale-up and time saving method that employs low cost solvent of precursors solution.

Although there are few reports on single Cu and Ni doped FeS_2 [29, 36], however, there is no such experimental report on the simultaneous Ni@Cu doped FeS_2 thin films. We have chosen Ni^{2+} and Cu^{1+} doping agents into pyrite FeS_2 due to facile and engineering optical properties without greatly perturbing the structure of FeS_2 lattice and thus avoiding the formation of thermodynamically unstable phases [37, 49, 50].

In this work the $Fe_{1-x}M_xS_2$ (M = Cu@Ni = 2, 5, 10, and 20 at %) semiconductor thin films are deposited by cost effective versatile chemical spray pyrolysis (CSP) deposition pertinent to photovoltaic applications. We report on the structural and surface properties of the simultaneous transition metal (M = Cu@Ni) doped FeS_2 system in the thin films form as well as fully evaluating the effect of doping on the optical properties. Engineering the band gap of FeS_2 using simultaneous Ni@Cu doping potentially makes it possible to use in multijunction based optoelectronic devices basically wide to narrow band gaps to increase the efficiency by capturing more of the solar spectrum. The prepared thin films are characterized by different characterization techniques.

EXPERIMENTAL DETAILS

Substrates Cleaning and Chemicals

The microscopic glass slides were used as substrates with thicknesses of 0.9–1.2 mm and dimensions of 3 by 2.5 cm. The substrates were subsequently cleaned in detergent soap, acetone, ethanol and deionized water with the assistance of agitation each for 15 min and finally dried in fresh air.

For the growth of $Fe_{1-x}M_xS_2$ (M = Ni@Cu) thin films, iron chloride ($FeCl_2$), thiourea (CH_4N_2S), copper chloride (CuCl), and nickel chloride ($NiCl_2$) were used as the sources of Fe, S, Ni^{2+}, and Cu^1. All required chemicals were purchased from MERCK Germany with the highest available purity.

$Fe_{1-x}M_xS_2$ Thin Films Growth

In the present study, the $Fe_{1-x}M_xS_2$ thin films (M = Ni@Cu) are synthesized using a versatile; low-cost and environmentally friendly chemical spray pyrolysis technique and the growth process of the thin films is describe as follows:

The undoped and Ni@Cu doped FeS_2 thin films are deposited in two steps. In the first step, 0.1 M of $FeCl_2$ and 0.2 M of CH_4N_2S are dissolved in distilled water. The solution is stirred on a hot plate with a constant stirring speed until (generally 1 h) becomes uniform transparent solution. Then, the solution is kept in a beaker and sprayed at a flow rate for 0.2 mL/min for 30 min on a microscopic clean glass substrate kept at a temperature of 290°C. After that, the film was kept in 20 min at 350°C and then it's cooled down slowly to room temperature to remove residual solvents and to form FeS_2 solid film. For Ni and Cu doping in FeS_2, the $NiCl_2$ (Ni = 1, 2.5, 5.0, and 10 at %) and the CuCl (Cu = 1, 2.5, 5.0, and 10 at %) reagents are mixed sequentially with the $FeCl_2$ (Fe = 98, 95, 90, and 80 at %) and (0.2 M) thiourea (CH_4N_2S) solution, respectively. Then the mixed solution is stirred as before, and then sprayed onto a glass substrate to deposit $Fe_{98}Ni_1Cu_1S_2$ thin film. The process is repeated for the deposition of the rest thin films followed by same stirrer and spraying conditions. All the parameters are kept unchanged throughout the whole experiment. The following reactions could be taken place on the heated substrates as:

$$\text{A.}\quad FeCl_2 + CH_4N_2S + H_2O \xrightarrow[\text{Decomposes}]{290^\circ C} FeS_2 + 2CO_2\uparrow + 2CH_4\uparrow + HCl\uparrow + NH_3\uparrow + 2\text{Steam}\uparrow,$$

B. $Fe_{1-x}Cl_2 + CH_4N_2S + Ni_xCl_2 + Cu_xCl + H_2O \xrightarrow[\text{Decomposes}]{290^\circ C} Fe_{1-x}M_xS_2 + 2CO_2\uparrow + 2CH_4\uparrow + HCl\uparrow + NH_3\uparrow + 2Steam\uparrow.$

Characterization

The morphology of the thin films was characterized by field-emission scanning electron microscope (FE-SEM, Philips) and the energy dispersive X-ray (EDX) data were also collected by this system at an accelerating voltage 10 kV. The chemical compositions and chemical states of the samples were investigated using X-ray photoelectron spectroscopy (XPS) (XPS; PHI) and the binding energies were calibrated according to the reference C 1*s* peak at 284.6 eV. The phase structures were examined using a powder X-ray diffraction (p-XRD) measurement on a D2 PHASER instrument with CuK_α radiation (λ = 0.15418 nm). The thin films were mounted flat and scanned in between $2\theta = 10^\circ$ and 80° with a step size of 0.02°. The optical properties were carried out using the spectroscopy ellipsometry (SE) data fitted with model data. Room temperature SE spectra (the amplitude ratio ψ, and the phase difference Δ) are measured in the spectral range of 190 to 1790 nm (0.73 to 6.5 eV) using a rotating-compensator instrument (J. A. Woollam, M-2000). The angle of incidence is varied from 55° to 75° with an increment of 5°. The back side of the glass substrate is taped with translucent plastic tape to eliminate back-side reflection [51]. The rotating compensator ellipsometer provides accurate results for the ellipsometric parameters ψ and Δ over the complete measurement range ($\psi = 0^\circ$–90°, $\Delta = 0^\circ$–360°). The transmission data of the samples were also collected in the same wavelength ranges.

RESULTS AND DISCUSSION

SEM and EDX

The surface morphology of the as-deposited *M* doped FeS_2 thin films was characterized using FE-SEM for varying concentration of the dopant precursors *M*. Figures 1a–1e show the FE-SEM images of FeS_2 and Ni@Cu-doped FeS_2 thin films. The films surfaces are continuous, uniformly distributed over the whole substrate surface indicates high material yield. Overall, the surface morphology of the thin films shows compact, adherent and crack/fracture free surfaces. It seems that the flat surfaces are composed of granular size grains and the granular grain sizes are uniformly distributed over the substrates. The granular grain size changes with Ni@Cu doping concentrations indicating that the morphology of $Fe_{1-x}M_xS_2$ (*M* = Ni@Cu) depends on the dopant concentration, i.e., effects on the grain growth FeS_2. These results are consistent with the report [36]. The increase of the granular sizes as with Ni@Cu doping is attributed to the increase of incorporation of Ni@Cu in FeS_2 crystal and increase the surface roughness consequently the Ni@Cu dopant ions hinder the FeS_2 crystal growth which is consistent with XRD results and other reports [31, 33]. The film surface seems to be roughest and coarse particles for *M* = 20 at % (Ni@Cu = 20 at %) doping (Fig. 1e) could be due to incomplete incorporation of Ni@Cu into FeS_2 lattice. The crystalline quality, morphology and texture are associated with the thin film surface roughness.

The chemical compositions of the thin films were investigated using energy dispersive X-ray (EDX) analysis (Figs. 2a, 2b). Two elemental peaks of Fe and S are observed in the EDX spectrum for FeS_2 film confirmed the compositions of undoped film is composed of Fe and S (Fig. 2a). In particular, two extra peaks of Ni and Cu are clearly observed along with the Fe and S atoms in the Ni@Cu doped FeS_2 sample indicate that at least parts of Ni and Cu were incorporated into FeS_2 crystal which is consistent with our expected result (Fig. 2b).

X-Ray Photoelectron Spectroscopy (XPS)

The high resolution XPS measurements were performed for qualitative analysis of pure FeS_2 (Figs. 3a, 3b) and Ni@Cu = 20% doped FeS_2, i.e., $Fe_{80}Ni_{10}Cu_{10}S_2$ (Fig. 3a'–3d') samples in the range of the binding energy of the constituent elements. It was taken to quantify chemical compositions, chemical states, purity, oxidation and/or the presence of other phases. The fitted binding energies for Fe 2*p*, S 2*p*, Ni 2*p*, and Cu 2*p* are presented in Table 1. Figures 3a, 3b show the high resolution wide-scale spectra of the elements, Fe and S for pure FeS_2 and their binding energies. From Fig. 3a, it can be seen four peaks are necessary to fit the Fe 2*p* peak signal at 709.40, 710.99, 717.66 and 723.50 eV (Table 1). The fitted double peak at 709.40 and 723.50 eV could be attributed to spin-orbit coupling of Fe $2p_{3/2}$ and Fe $2p_{1/2}$ states which are consistent with the energies expected for FeS_2 [52–57]. The second peak centered at 710.99 eV and the satellite peak at 717. 66 eV can be assigned to Fe^{3+}–S or Fe^{3+}–O resulting from surface oxidation intermediates [52–58]. These iron oxide (FeO) or $Fe(SO_4)_3$ species are generated on the films surfaces during the cooling of the sample at the atmospheric conditions. However, these impurities were not identified by XRD analysis (Fig. 4), either because of their very low degree of crystallization or they were present as very thin layer on the surface of pyrite crystals [52, 53]. Whereas, the S 2*p* state typically splits into two components at the binding energies of 167.57 eV (S $2p_{1/2}$) and 168.61 eV (S–O bond) (Fig. 3b, Table 1) which are larger binding energy than the standard binding energy of S 2*p* states. This higher binding energy of S 2*p* state is due to the oxidation of the sample and indicates the presence of S–O bond in the sample. While for Ni@Cu = 20%

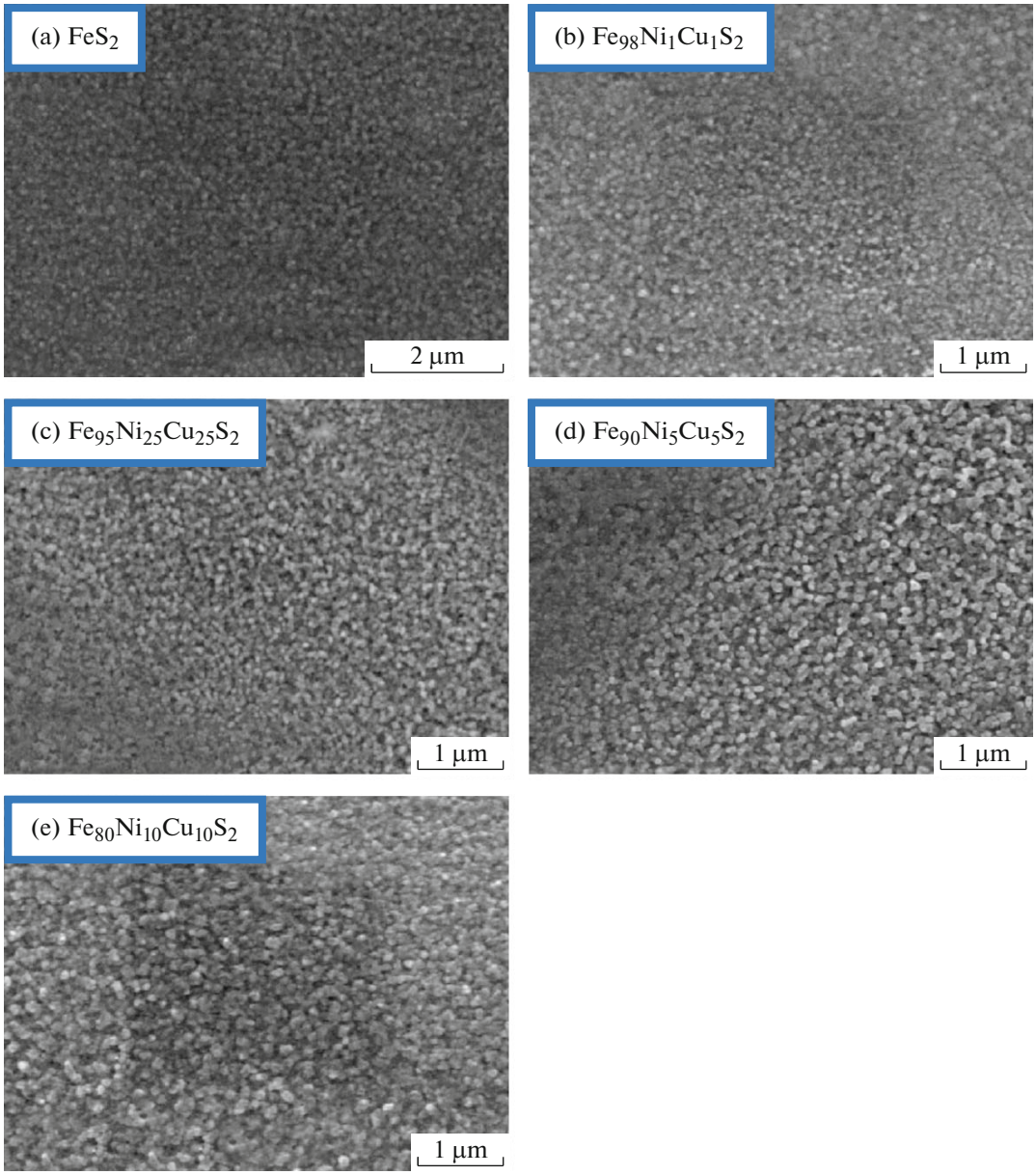

Fig. 1. FE-SEM images of $Fe_{1-x}M_xS_2$ for (a) Ni@Cu = 0.0, (b) Ni@Cu =1.0 + 1.0 = 2.0%, (c) Ni + Cu = 2.5 + 2.5 = 5.0%, (d) Ni@Cu = 5.0 + 5.0 = 10.0%, and (e) Ni@Cu = 10.0 + 10.0 = 20 at % thin films.

doping FeS_2 (Figs. 3a'–3d', Table 1) sample, the Fe 2*p* state splitting into four chemical states at the binding energies of 709.64, 711.32, 718.16, and 723.88 eV (Fig. 3a'). The deconvolution peaks centered at energies of 709.64 and 723.88 eV are due to Fe $2p_{3/2}$ and Fe $2p_{1/2}$. The presence of peaks at the binding energies ~711.32 and 718.16 eV is ascribed to Fe^{3+} which demonstrates that the Fe edges in FeS_2 were slightly oxidized during the transition from the state Fe^{2+} to the state Fe^{3+}. Whereas, two peaks are observed in the S 2*p* spectrum (Fig. 3b', Table 1); one at the binding energy 167.75 eV is due to S $2p_{1/2}$ and another at the binding energy 168.85 eV corresponds to the presence of S–O bond [59]. Presence of the S–O bond in $Fe_{80}Ni_{10}Cu_{10}S_2$ insights a partial oxidation was occurred of the S edges in $Fe_{80}Ni_{10}Cu_{10}S_2$ thin film. It is interesting that the Cu 2*p* state is fitted with two very high intense peaks centered at the binding energies of 932.19 and 952.08 eV correspond to Cu $2p_{3/2}$ and Cu $2p_{1/2}$ states (Fig. 3c'), respectively. The presence of the Cu2 $p_{3/2}$ and Cu $2p_{1/2}$ states in the spectrum indicates that Cu was incorporated into FeS_2 lattice [58]. In case of Ni element, the Ni 2*p* core-level (Fig. 3d') shows two intense peaks around at the binding energies of 866.81 and 877.17 eV. The peak at 877.17 eV

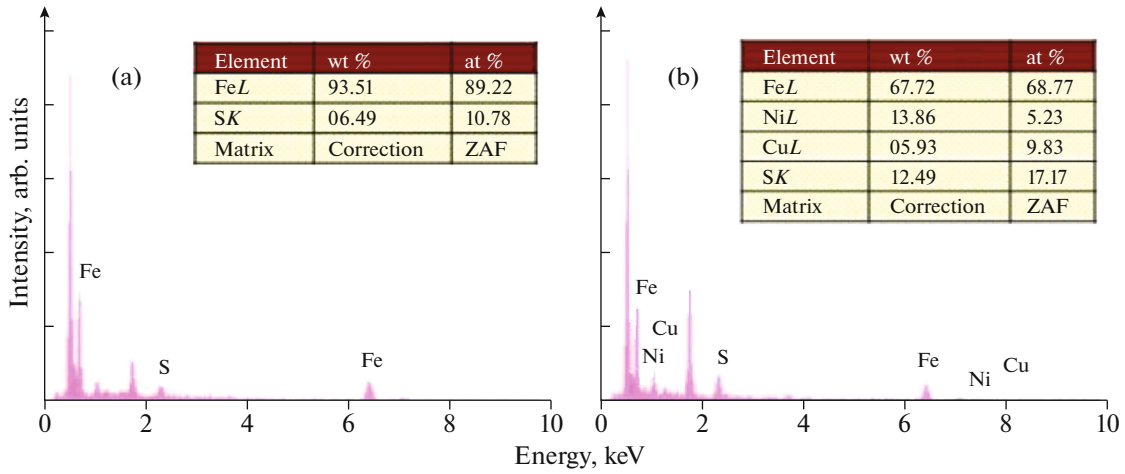

Fig. 2. EDX spectrum for (a) FeS_2 and (b) $Fe_{80}Ni_{10}Cu_{10}S_2$ thin films.

is attributed to Ni $2p_{1/2}$. However, the satellite peak at ~866.81 eV (Ni $2p_{3/2}$) is attributed due to oxide phase formation of Ni [60]. It should be noted that all the peaks position are slightly shifted toward higher energy from the standard values. However, for Ni@Cu doping the binding energy is more shifted toward higher energy could be attributed due to more reactive of $Fe_{1-x}M_xS_2$ surface oxidation than undoped FeS_2 [61–63]. It is reported that pyrite containing impurities observed to be more reactive than undoped pyrite [61–63] and hence M doped FeS_2 exhibiting the shifting of binding energies of surface components toward higher energies as compared to pure FeS_2 [64].

X-Ray Diffraction (XRD)

To investigate the phases and purities of the $Fe_{1-x}M_xS_2$ samples, the XRD data were collected in the range of 10°–80° shown in the Fig. 4 and the data were analyzed very carefully using different formula. All the diffraction peaks are observed in these patterns can be indexed as pyrite FeS_2 (ICDD 71-1680). The diffraction peaks at (111), (210), (211), (220), and (311) reflections planes attributed to the cubic structure of FeS_2. No other impurities peaks (such as marcasite FeS, FeSe etc.) were observed in the patterns indicated that the deposited samples are pure FeS_2. The intensity of the peak (111) decreases with increasing Ni@Cu indicating that the crystallinity decreases which is consistent with the SEM, band gap results and report [21]. The narrow peak at 29.67° illuminated the crystallization nature of the samples. It should be noted that the Fe^{2+} cations occupy the sites of a face centered- cubic sublattice, and the $(S_2)^{2-}$ dimers are centered at the midpoints of the cube edges. The axes of the $(S_2)^{2-}$ dimers are oriented along the [111] direction; each Fe atom is coordinated to six sulfurs in a slightly distorted-octahedron structure and each S atom is bonded to three Fe atoms and dimer pair (not shown here). From this Fig. 4 it is evidenced that FeS_2 preferentially grown along (111) plane. However, the diffraction peaks are broad, weak, and fluctuating, indicating that the samples have low purity and crystallinity, i.e., amorphous phase coexists with crystalline phase in the samples due to low growth temperature. The lattice constant, 'a' is calculated using the following relation (1):

$$\frac{1}{d_{hkl}^2} = \frac{h^2 + k^2 + l^2}{a^2}. \quad (1)$$

The estimated parameters lattice constant, volume and lattice strain are presented in Table 2. The estimated values of *a* are in good agreement with the published values [65].

Table 1. Binding energy of the different elements of $Fe_{1-x}M_xS_2$ thin films

Sample	Binding energy (eV) of the films constituent elements							
	Fe		S		Cu		Ni	
	Fe $2p_{3/2}$	Fe $2p_{1/2}$	S $2p_{1/2}$	S–O	Cu $2p_{3/2}$	Cu $2p_{1/2}$	Ni $2p_{3/2}$	Ni $2p_{1/2}$
FeS_2	709.40	723.50	167.57	168.61	—	—	—	—
$Fe_{00}Ni_{10}Cu_{10}S_2$	709.64	723.88	167.75	168.85	932.19	952.08	866.81	877.17

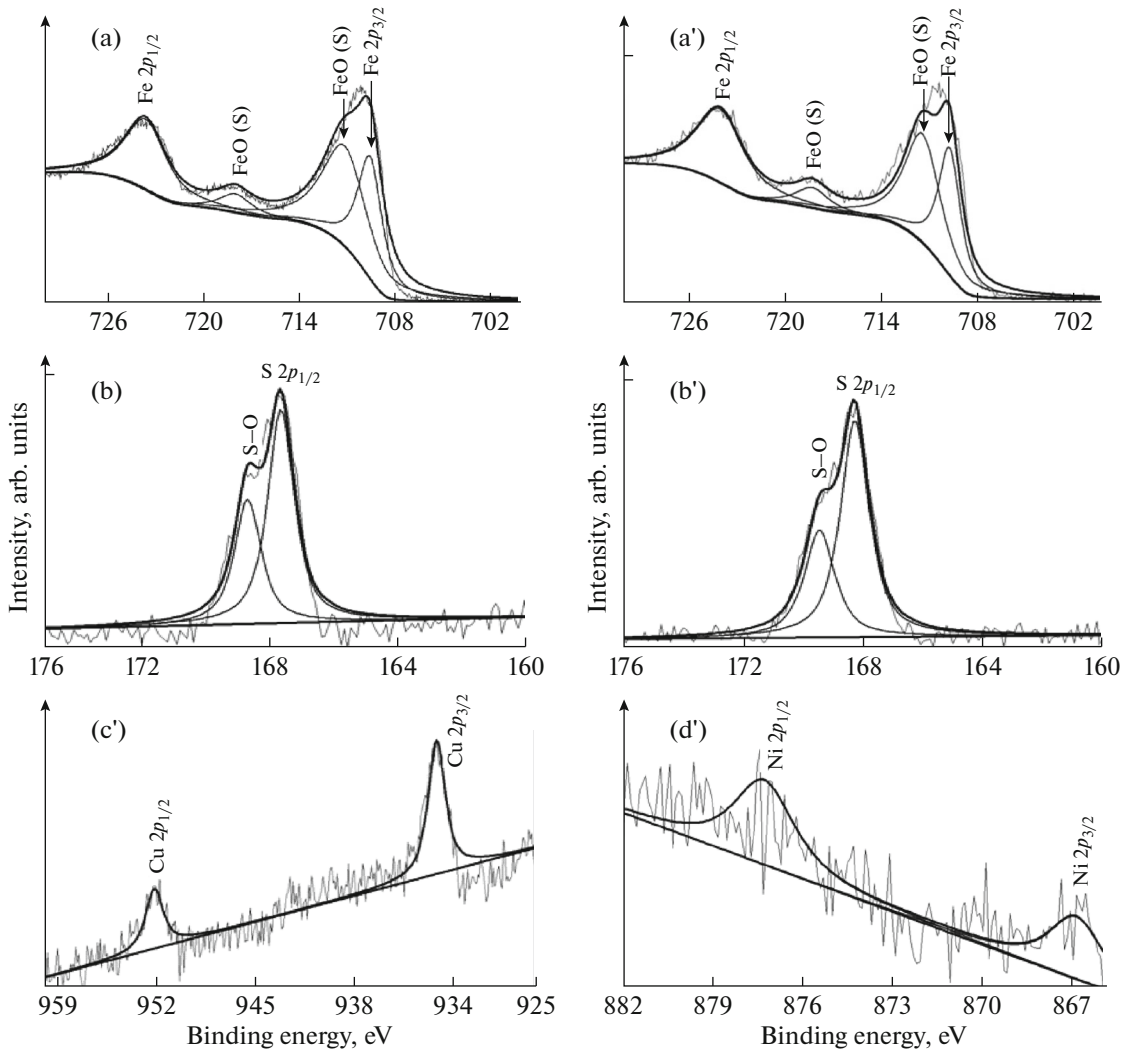

Fig. 3. High resolution XPS spectra of (a, b) FeS_2 and (a'–d') $Fe_{80}Ni_{10}Cu_{10}S_2$ thin films.

The average grain size of the films was found out using the Scherrer's formula [66]

$$L_g = \frac{0.9\lambda}{\beta\cos\theta}, \quad (2)$$

where L_g is the average grain size, λ is the X-ray wavelength of CuK_α (λ = 1.5406 Å), β is the full width at half maximum (FWHM) expressed in radian, and θ is Bragg angle in degree. It could be found that the average crystallite size lies in between 76 and 18 nm.

Optical Constants and Band Gap

The investigation of the optical properties is an essential part of this research work. The production of high-quality thin films, and enhancement of the absorption coefficient and optical band gap could be a

Table 2. Lattice constants, volume, crystallite size and lattice strain of $Fe_{1-x}M_xS_2$ thin films

Sample's name	Lattice constant, *a*, Å	Volume, Å^3	Average crystallite size, nm	Lattice strain
FeS_2	5.281	147.287	76.00	0.197
$Fe_{98}Ni_1Cu_1S_2$	5.273	146.623	36.30	0.393
$Fe_{95}Ni_{2.5}Cu_{2.5}S_2$	5.260	145.541	21.40	0.655
$Fe_{90}Ni_5Cu_5S_2$	5.279	147.151	17.40	0.788
$Fe_{80}Ni_{10}Cu_{10}S_2$	5.264	145.856	76.00	0.196

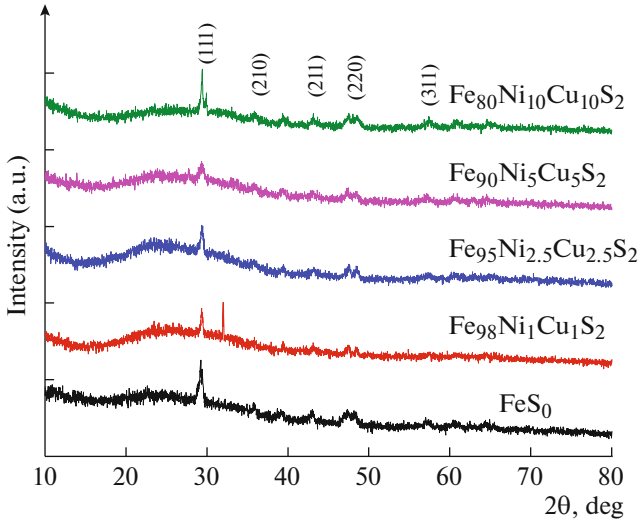

Fig. 4. XRD patterns of $Fe_{1-x}M_xS_2$ thin films.

solution to enhance the performance of pyrite based optoelectronic devices; basically the solar cell devices [36, 37]. To this point of view, a high powerful spectroscopic ellipsometry technique is used to collect the spectra (phase, Δ and amplitude, Ψ) for Kramers-Kronig analysis. From these spectra the optical constants $n(\omega)$ and $\kappa(\omega)$, the real $\varepsilon_1(\omega)$ and imaginary $\varepsilon_2(\omega)$ parts of the complex dielectric function $\varepsilon(\omega)$ as well as thickness (t) of the samples were determined after fitting a model using software packages Complete EASE® so that the parameters of the model are adjusted to match the theoretical and experimental ψ and Δ values of the film material [51, 67, 68]. The interpolation B-spline model was used to adjust the parameters. After goodness of fit, the graphs were clipboarded which are shown in Figs. S1a–S1d (fitted phase, Δ and amplitude, Ψ), Figs. S2a–S2d (example: fitted with expt. (a) refractive index, (b) real dielectric constant, (c) imaginary dielectric constant, and (d) extinction coefficient), Figs. S3a–S3d (transmittance fitted with expt.) and Fig. S3e (fitted transmittance result), respectively. The fitting procedure is described in the Supplementary Materials. The fitted obtained results are described in the following.

The refractive index n describes changes to light wave caused by interaction with materials. In general for nonmagnetic substances, $n(\omega) = \sqrt{\varepsilon(\omega)}$ which is very useful for relating the dielectric properties of a material to its optical properties at any particular frequency of interest. Since n depends on the wavelength of light, thus $\sqrt{\varepsilon}(\omega)$ depends on it too, which is so called dispersion. The complex refractive index, N with real part n and imaginary part κ (so called extinction coefficient), is related to the complex permittivity

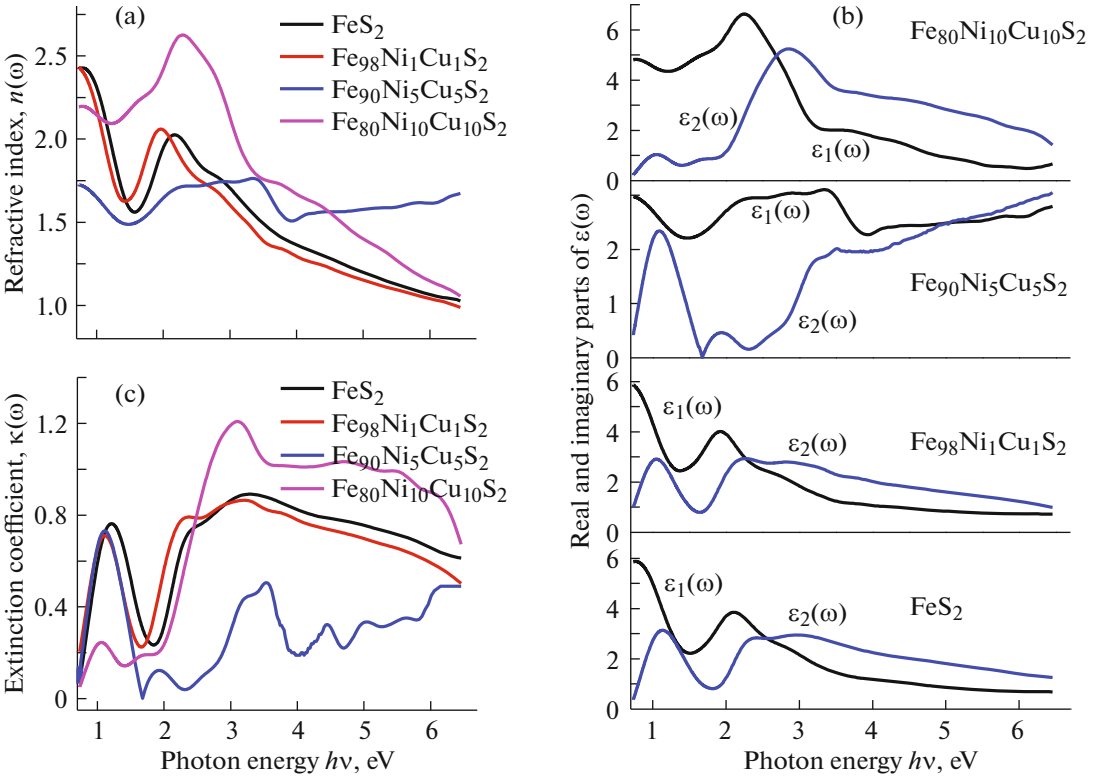

Fig. 5. Results of (a) refractive index, $n(\omega)$, (b) complex dielectric function, $\varepsilon(\omega)$, and (c) extinction coefficient, $\kappa(\omega)$ of $Fe_{1-x}M_xS_2$ thin films.

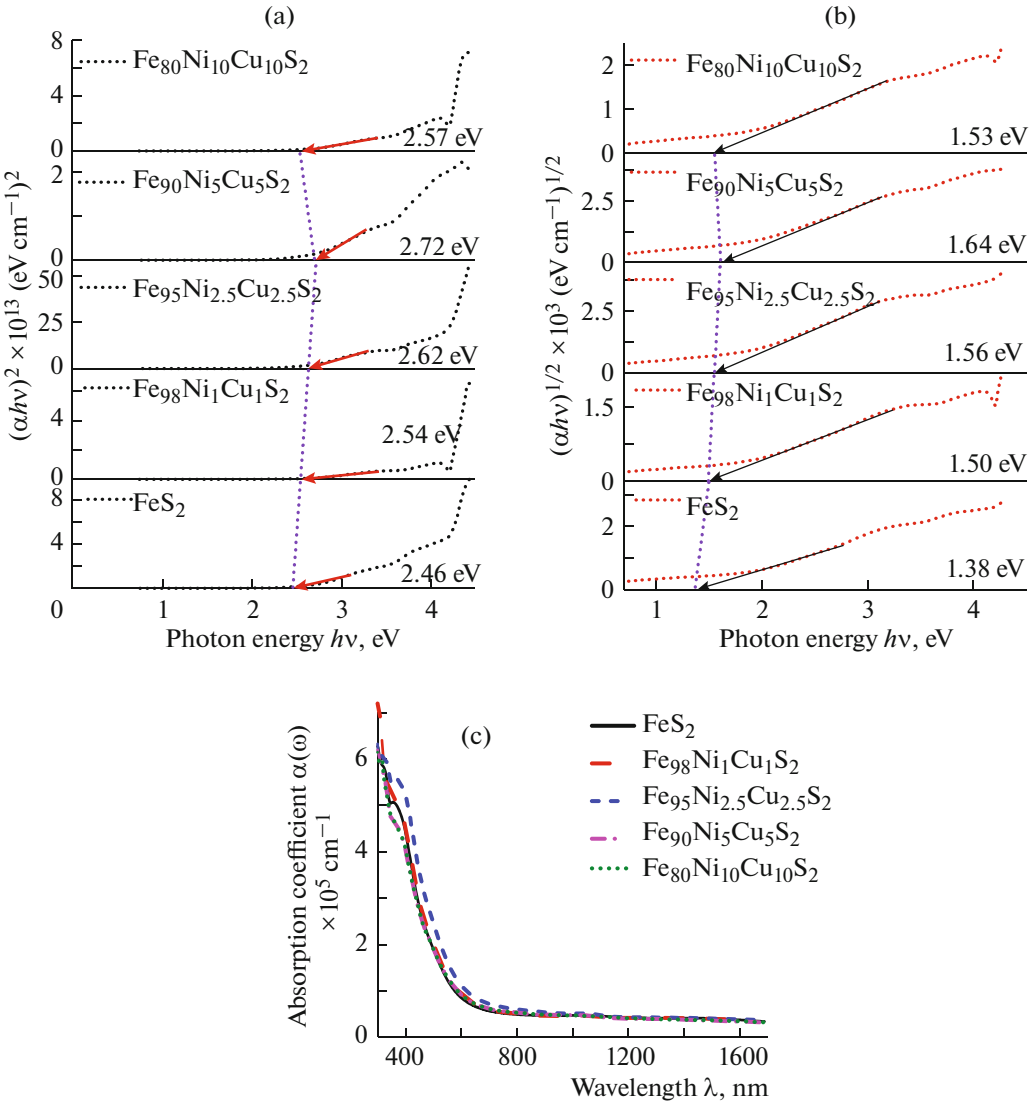

Fig. 6. Tauc plots of $Fe_{1-x}M_xS_2$ thin films for determination of (a) direct and (b) indirect band gap. (c) Absorption coefficient, $\alpha(\omega)$ of $Fe_{1-x}M_xS_2$ thin films.

as, $\epsilon(\omega) = \epsilon_1(\omega) - i\epsilon_2(\omega)$ and $N(\omega) = n(\omega) - i\varkappa(\omega)$, where real part n is called refractive index and imaginary part κ is called the extinction coefficient. Thus, $\varepsilon(\omega) = N^2(\omega)$, $\varepsilon_1(\omega) = n^2(\omega) - \varkappa^2(\omega)$ and $\epsilon_2(\omega) = 2n(\omega)\varkappa(\omega)$.

Figure 5a represented the refractive index, $n(\omega)$ of the thin film samples. The refractive index shows well dispersive nature for each sample and the value reaches maximum at a certain energy indicating the large polarization induced in that energy. After reaching in maximum, the value of $n(\omega)$ decreases with increasing photon energy attribute due to different loss mechanism participation. It should be noted that $n(\omega)$ is inter-related to the local polarizability as well as the electronic density of the investigated thin films. The value of the refractive index, $n(\omega)$ at zero energy ($\omega = 0$) is obtained to be ~1.98, 2.0, 3, 4.5, 6.0, and 3.02 for undoped and Ni@Cu-doped FeS_2 thin films, respectively. It is evident that at low energy, the value of $n(\omega)$ decreases with increasing Ni@Cu doping concentration which is related to well-known an inverse width of the optical band gap describe by Penn model [69]. The results are consistent with the band gap energies of the thin film samples.

Figure 5b shows the variation of the real $\varepsilon_1(\omega)$ and imaginary $\varepsilon_2(\omega)$ dielectric functions with doping as a function of photon energy (ω). The static dielectric constant, $\varepsilon(0)$ of FeS_2 decreases with increasing of Ni@Cu doping insights an increase of the band gap. The real dielectric function $\varepsilon_1(\omega)$ is high at lower energies attributed to all types of polarizations can be effective implying that an electric field can easily

polarize these materials at lower photon energy. In contrast, the imaginary dielectric function, $\varepsilon_2(\omega)$ is just opposite nature to $\varepsilon_1(\omega)$. It can be clearly seen a good dispersive nature of $\varepsilon_1(\omega)$ for each thin film and the maximum value of $\varepsilon_1(\omega)$ reaches at a certain energy insights maximum polarization can occur in that electric field energy. The peak position is shifted toward higher energy with Ni@Cu doping indicates that more polarization can be introduced by Ni@Cu and the at least a part of Ni@Cu was incorporated into FeS_2 lattice. After reaching in maximum, the value of $\varepsilon_1(\omega)$ decreases as with increasing of photon energy (ω) attributed due to some of the polarization may not be effective and hence the value of $\varepsilon_1(\omega)$ at higher energy may be quite small as compared to static value. The dielectric loss occurs after a certain energy could be due to the lag of polarization and additional to various loss mechanisms such as: the generation of phonons (lattice waves), photogeneration, free-carrier absorption and scattering, etc. The real part dielectric function, $\varepsilon_1(\omega)$ decreases with increasing doping concentration is in good agreement with the report [21]. The real dielectric function, $\varepsilon_1(\omega)$ showed lower value than the theoretical report [21] could be due to the effect of the morphology factor (grain size, grain direction, density of the materials, etc.) [70]. The effects of grain size, grain orientation, defects and lattice constants were neglected in the theoretical study [21] and there was only considered the defect free structure in the bulk form. It should be remember that the effective dielectric function in the Yamada equation is greatly affected by the change of the morphology factor [70]. A small change of the morphology factor gives a large difference in the dielectric function [70].

On the other hand, the imaginary dielectric function, $\varepsilon_2(\omega)$ increases with increasing photon energy (ω) and a peak arises at 1.25 eV (Fig. 5b) is due to the optical transition from the hybridization upper valence band Fe 3*d* and S 3*p* orbitals to the lowest conduction band mixed Fe 3*d* and S 3*p* orbitals. Whereas, a critical peak arises at ~ 3.20 eV is assigned to optical transitions in between deep Fe 3*d* state to upper conduction mixed Fe 3*d* and S 3*p* states. In case of Ni@Cu doping, the peak at ~ 3.20 eV arises due to the optical transition from the hybridization valence band Fe 3*d* Ni 3*d* and Cu 3*d* states to the upper hybridization conduction band Ni 3*d* and Fe 3*d* states. The optical transition from the hybridization of valence band Fe *d* and S *p* states to the lowest conduction band S *p* and Fe *d* states, respectively [71]. The peak at ~3.20 eV is due to the optical transition from the valence band Fe *d* and S *p* states to the lowest conduction band of Ni *d* and S *p* and Fe *d* states, respectively [21].

The absorption coefficient, $\alpha(\omega)$ is determined from the transmittance fitting data (shown in Figs. S3a–S3e, Supplementary Materials) using the relation, $\alpha = -\ln T/t$, where T is the transmittance (shown in Fig. S3, Supplementary Materials) and t is the thickness ($t = 371 \pm 12$, 377 ± 17, 372 ± 13, 386 ± 12 nm, and corresponding roughness of the film, $r = 8$, 17, 28, and 42 nm) nm of the samples. The variation of the absorption coefficient with wavelength is shown in Fig. 6c. It is evident that the absorption coefficient increases with increasing of Ni@Cu doping up to 10 at %, however, at higher doping concentration it deteriorate could be due to structural change and/or Ni, Cu ions cannot completely incorporate into FeS_2 lattice [21]. It can be observed that the absorption coefficient exhibits minimum value around ~1000 nm insights the band gap of the films material could be located around this region, however the absorption coefficient increases linearly in the visible region ~650 nm to near ultraviolet region. Thus enhancing the optical response in Ni@Cu doped FeS_2 alloys in performance acting as a *p*-type semiconductor proposed in [72]. Henceforth, the absorption coefficient spectra of alloys have transposed with that of iron pyrite. The result of optical absorption agreed with [73, 74].

The optical transition nature of a thin film material can be determined by the relationship between the absorption coefficient (α) and the energy of the incident photon ($h\nu$) using Tauc's relation [75] as:

$$\alpha h\nu = A(h\nu - E_g)^n, \quad (3)$$

where E_g is the band gap energy and A is a constant related to the effective masses associated with the valence band and the conduction band, and n is the power factor. The value of n is assumed to be 1/2, 2, 3/2, and 3 for allowed direct, allowed indirect, forbidden direct, and forbidden indirect transitions, respectively. Here we calculate for allowed direct ($n = 1/2$) and indirect ($n = 2$), respectively as follows:

$$\alpha h\nu = A(h\nu - E_g)^{1/2} \quad (4)$$

and

$$\alpha h\nu = \mathrm{A}(h\nu - E_g)^2. \quad (5)$$

Using Eqs. (4) and (5) the direct and indirect band gap energies of the films are determined from the intercept on the energy axis after extrapolation of the straight line section of the Tauc plots $(\alpha h\nu)^2$ vs. $h\nu$ (photon energy) and $(\alpha h\nu)^{1/2}$ vs. $h\nu$ (photon energy) curves (Figs. 6a, 6b), respectively. The direct and indirect optical band gaps of FeS_2 obtained to be $E_g = 2.46$ and 1.38 eV which is very close to the reported results [36, 37]. The band gap energy is being progressive shift (direct and indirect) from 2.46 to 2.72 and 1.38 to 1.64 eV (Table 3) while the concentration of Ni@Cu is increased from 0 to 10 at %. However, at higher Ni@Cu = 20 at % doping concentration, the band gap is reduced (Table 3) could be due to crystal structure change and/or improper impurity doping which is good agreement with the SEM, XRD and optical constants results. A blue shifts in the band edge shows the formation of solid solution [21, 76, 77], however, the

Table 3. Direct and indirect band gap energies of $Fe_{1-x}M_xS_2$ thin films

Sample's name	Value of direct band gap, eV	Value of indirect band gap, eV
FeS_2	2.46	1.38
$Fe_{98}Ni_1Cu_1S_2$	2.54	1.50
$Fe_{95}Ni_{2.5}Cu_{2.5}S_2$	2.62	1.56
$Fe_{90}Ni_5Cu_5S_2$	2.72	1.64
$Fe_{80}Ni_{10}Cu_{10}S_2$	2.57	1.53

variation of the optical gap is not so much attributed due to limited solubility [78] of Ni atom rather than Cu into FeS_2. In Ni doped FeS_2 an irregular band gap variation with mol % variation is also exhibited by Sadia Khalid et al. [36, 37]. The change of the band gap value is sensitive to small changes in carrier concentration, grain size, defects and film stress. With the increase of granular size, the band gap widening is observed could be attributed to the local electric fields originated from the impurity or carriers density which lead to affect the band tails near the band edge [13, 79]. Importantly, when Ni@Cu is doped in FeS_2, it can be incorporated into interstitial and/or substitution. If Ni and Cu are incorporated into intestinal sites, it makes free electrons like, $Ni^{2+} \rightarrow 2e$ and $Cu^{+} \rightarrow e$ impurities layers below the conduction band resulting in band gap could be decreased. Since the band gap is increased, there is a possibility of substation of Ni^{2+} (0.069 nm) and Cu^{1+} (0.073 nm) on Fe^{2+} (0.065 nm) sites then the impurity levels $Ni_{Fe} \rightarrow 2e$ and $Cu_{Fe} \rightarrow h^{+}$ introduced just below the conduction band minimum in case of Ni doped and valence band maximum for Cu doped which excellent agreement with the reports [21, 34]. It is reported that the valence band maximum (VBM) and conduction band minimum (CBM) are formed by 3*d* orbitals of Fe atom and the mixture of Fe 3*d* and S 3*p* states. When Ni and Cu is doped into FeS_2, the impurity bands are generated just below the CBM as a result of the mixture of Ni/Fe states revealing an upwards shift influenced by the crystal-field splitting while in the valence band maximum downward shift, the new bands are generated which are very tights and mainly constituted by the degenerated of Ni 3*d*, Fe 3*d* and Cu 3*d* states caused by additional levels of the Ni and Cu-electrons as a result the band gap is increased up to a limiting value of Ni@Cu doping concentration [21, 34]. Whereas, for Ni@Cu = 20 at % doping, the band gap reduced is observed qualified the existence of structural change by the down shifting of the conduction band and/or unstable of the system at higher Ni@Cu doping [21, 34] which is consistent with the XRD (Fig. 4), SEM (Fig. 1e) and with available works [28, 36, 37]. In this case Fe is to be reduced receiving electrons in its 3*d* orbitals and the Cu was mostly to be oxidized [80].

CONCLUSIONS

In this research work, the undoped FeS_2 and Ni@Cu doped FeS_2 thin films have been synthesized successfully by chemical spray pyrolysis process. The FE-SEM images exhibit that the film surface is compact and composed of granular like nanostructures grains. The granular size increases with the increases of Ni@Cu in FeS_2. The XRD results provide an evidenced of the formation of cubic crystal. The crystallinity of the films deteriorate with increasing Ni@Cu doping. The EDX and XPS measurements exhibit that the films are composed of Fe, S, Ni, and Cu elements and the films were slightly oxidized. The indirect band gap value of the Ni@Cu doped FeS_2 films are found to be gradually increased from 1.38 eV (FeS_2) to 1.64 eV (Ni@Cu = 20 at %). So, the direct band gap can be tuned in between 2.46 and 2.72 eV using co-doping Ni@Cu in FeS_2. Importantly, the absorption increases as with Ni@Cu doping in the visible and near ultraviolet regions which is an important property for optoelectronics applications. Therefore, the thin films deposited by chemical spray pyrolysis technique exhibit good structure and excellent optical properties which would be cost effective for optoelectronics basically solar cell device applications.

ACKNOWLEDGMENTS

Authors are thankful to the Ministry of Science and Technology (R& D ID no. 2280, 2018-2019, Physical Science), People's Republic of Bangladesh for financial support and City University of Hong Kong, Hong Kong SAR, P. R China for providing samples characterization facilities.

SUPPLEMENTARY MATERIALS

Supplementary materials are available for this article at https://doi.org/10.1134/S1063774520060188 and are accessible for authorized users.

REFERENCES

1. J. H. Zhao, A. H. Wang, M. A. Green, and F. Ferrazza, Appl. Phys. Lett. **73**, 1991 (1991).
2. A. Luque and S. Hegedus, *Handbook of Photovoltaic Science and Engineering* (Wiley, 2003).
3. H. J. Snaith, J. Phys. Chem. Lett. **4,** 3623 (2013).
4. A. Chirilă, S. Buecheler, F. Pianezzi, P. Bloesch, C. Gretener, A. R. Uhl, C. Fella, L. Kranz, J. Perrenoud, S. Seyrling, R. Verma, S. Nishiwaki, Y. E. Romanyuk, G. Bilger, and A. N. Tiwari, Nat. Mater. **10**, 857 (2011).
5. D. J. Lewis, P. Kevin, O. Bakr, C. A. Muryn, M. A. Malik, and P. O'Brien, Inorg. Chem. Front. **1**, 577 (2014).
6. D. J. Binks, Phys. Chem. Chem. Phys. **13**, 12693 (2011).
7. M. Kamruzzaman, Nanoscale Adv. **2**, 286 (2020).

8. M. Kamruzzaman, L. Chaoping, A. K. M. Farid Ul Islam, and J. A. Zapien, Semiconductors **51**, 1615 (2017).
9. M. Kamruzzaman and J. A. Zapien, J. Nanopart. Res. **19**, 125 (2017).
10. M. Kamruzzaman, L. Chaoping, F. Yishu, A. K. M. Farid Ul Islam, and J. A. Zapien, RSC Adv. **6**, 99282 (2016).
11. M. Kamruzzaman, J. Schneider, and J. A. Zapien, *Application of Nanostructured Materials for Energy and Environmental Technology* (2015), p. 125.
12. M. Kamruzzaman, R. Dutta, and J. Podder, Semiconductors **46**, 957 (2012).
13. M. Kamruzzaman, T. R. Luna, Jiban Podder, and M. G. M. Anowar, Semicond. Sci. Technol. **27**, 035017 (2012).
14. S. N. Malik, S. Mahboob, N. Haider, M. A. Malik, and P. O'Brien, Nanoscale **3**, 5132 (2011).
15. S. N. Malik, A. Q. Malik, R. F. Mehmood, G. Murtaza, Y. G. Alghamdi, and M. A. Malik, New J. Chem. **39**, 4047 (2015).
16. M. Azad Malik, N. Revaprasadu, and K. Ramasamy, *Nanomaterials for Solar Energy,* in *Nanoscience*: Vol. 1: *Nanostructures through Chemistry* (The Royal Society of Chemistry, 2013), p. 29.
17. D. A. Mazón-Montijo, M. T. S. Nair, and P. K. Nair, ECS J. Solid State Sci. Technol. **2**, 465 (2013).
18. X. Zhang, M. Manno, A. Baruth, M. Johnson, E. S. Aydil and C. Leighton, ACS Nano **7**, 2781 (2013).
19. M. Cabán-Acevedo, D. Liang, K. S. Chew, J. P. DeGrave, N. S. Kaiser, and S. Jin, ACS Nano **7**, 1731 (2013).
20. C. Wadia, Y. Wu, S. Gul, S. K. Volkman, J. Guo, and A. P. Alivisatos, Chem. Mater. **21**, 2568 (2009).
21. N. Ouarab, Phys. E (Amsterdam, Neth.) **115**, 113688 (2020).
22. V. Kumar Gudelli, V. Kanchana, S. Appalakondaiah, G. Vaitheeswaran, and M. C. Valsakuma, J. Phys. Chem. C **117**, 21120 (2013).
23. A. Schlegel and P. Wachter, J. Phys. C: Solid State Phys. **9**, 3363 (1976).
24. A. Ennaoui, S. Fiechter, Ch. Pettenkofer, N. Alonso-Vante, K. Büker, M. Bronold, Ch. Höpfner, and H. Tributsch, Sol. Energy Mater. Sol. Cells **29**, 289 (1993).
25. J. Puthussery, S. Seefeld, N. Berry, M. Gibbs, and M. Law, J. Am. Chem. Soc. **133**, 716 (2011).
26. A. Kirkeminde, R. Scott, and S. Ren, Nanoscale **4**, 7649 (2012).
27. S. Middya, A. Layek, A. Dey, and P. P. Ray, J. Mater. Sci. Technol. **30**, 770 (2014).
28. S. W. Lehner, K. S. Savage, and J. C. Ayers, J. Cryst. Growth **286**, 306 (2006).
29. J.-J. Wu, W.-K. Ma, F. Jiao, and W.-Q. Qin, Chin. J. Nonferrous Met. **27** (3), 605 (2017).
30. D. Banjara, Y. Malozovsky, L. Franklin, and D. Bagayoko, AIP Adv. **8**, 025212 (2018).
31. A. Hung, J. Muscat, I. Yarovsky, and S. P. Russo, Surf. Sci. **520**, 111 (2002).
32. T. Schena, G. Bihlmayer, and S. Blugel, Phys. Rev. B **88**, 235203 (2013).
33. R. Sun, M. K. Y. Chan, and G. Ceder, Phys. Rev. B **83**, 235311 (2011).
34. J. Fan and S. Lu, Adv. Mater. Res. **652–654**, 590 (2013).
35. J. Hu, Y. Zhang, M. Law, and R. Wu, J. Am. Chem. Soc. **134**, 13216 (2012).
36. S. Khalid, M. A. Malik, D. J. Lewis, P. Kevin, E. Ahmed, Y. Khan, and P. O'Brien, J. Mater. Chem. C **3**, 12068 (2015).
37. S. Khalid, E. Ahmed, M. A. Malik, D. J. Lewis, S. A. Bakar, Y. Khan, and P. O'Brien, New J. Chem. **39**, 1013 (2015).
38. M. Zhang, B. Chen, H. Tang, G. Tang, C. Li, L. Chen, H. Zhang, and Q. Zhang, RSC Adv. **5**, 1417 (2015).
39. P. Prabukanthan, S. Thamaraiselvi, and G. Harichandran, J. Electrochem. Soc. **164** (9), D581 (2017).
40. C. T. Kao, J. B. Shi, H. W. Lee, F. C. Cheng, H. H. Liu, M. W. Lee, C. C. Chan, C. W. Huang, H. S. Lin, P. F. Wu, C. Y. Chen, M. C. Kao, S. L. Young, and C. L. Lin, J. Therm. Spray Technol. **25**, 580 (2016).
41. S. Bausch, B. Sailer, H. Keppner, G. Willeke, E. Bucher, and G. Frommeyer, Appl. Phys. Lett. **57**, 25 (1990).
42. K. Sun, Z. Su, J. Yang, Z. Han, F. Liu, Y. Lai, J. Li, and Y. Liu, Thin Solid Films **542,** 123 (2013).
43. M. Birkholz, D. Lichtenberger, C. Höpfner, and S. Fiechter, Sol. Energy Mater. Sol. Cells **27**, 243 (1992).
44. H. Dahman, M. Khalifa, M. Brunel, and B. Rezig, Thin Solid Films **280**, 56 (1996).
45. B. Thomas, K. Diesner, T. Cibik, and K. Ellmer, Solid State Phen. **51–52**, 301 (1996).
46. N. Berry, M. Cheng, C. L. Perkins, M. Limpinsel, J. C. Hemminger, and M. Law, Adv. Energy Mater. **2**, 1124 (2012).
47. J. Hu, Y. Zhang, M. Law, and R. Wu, Phys. Rev. B: Condens. Matter Mater. Phys. **85**, 1 (2012).
48. M. Bronold, S. Kubala, C. Pettenkofer, and W. Jaegermann, Thin Solid Films **304**, 178 (1997).
49. C. Ho, C. Huang, and C. Wu, J. Cryst. Growth **270**, 535 (2004).
50. Y. Tomm, R. Schieck, K. Ellmer, and S. Fiechter, J. Cryst. Growth **146**, 271 (1995).
51. R. A. Synowicki, Phys. Status Solidi C **5**, 1085 (2008).
52. D. Wang, Q. Wang, and T. Wang, Cryst. Eng. Comm. **12**, 3797 (2010).
53. M. V. M. Gallardo, A. M. Ayala, M. Pal, M. A. C. Jacome, J. A. T. Antonio, and N. R. Mathews, Chem. Phys. Lett. **660**, 93 (2016).
54. A. Ennaoui, S. Fiechter, W. Jaegermann, and H. Tributsch, J. Electrochem. Soc. **133**, 97 (1986).
55. C. M. Eggleston, J.-J. Ehrhardt, and W. Stumm, Am. Miner. **81**, 1036 (1996).
56. P. Mills and J. L. Sullivan, J. Phys. D: Appl. Phys. **16**, 723 (1983).
57. Y. Cai, Y. Pan, J. Xue, Q. Sun, G. Su, and X. Li, Appl. Surf. Sci. **255**, 8750 (2009).
58. B. Li, L. Huang, M. Zhong, Z. Wei, and J. Li, RSC Adv. **5**, 91103 (2015).
59. X. J. Lv, G. W. She, S. X. Zhou, and Y. M. Li, RSC Adv. **3**, 21231 (2013).

60. Z.-L. Ma, R.-L. Jia, and C.-J. Liu, J. Mol. Catal. A: Chem. **210**, 157 (2004).
61. Y.-Q. Li, J.-H. Chen, Y. Chen, and J. Guo, Trans. Nonferrous Met. Soc. Chin. **21**, 1887 (2011).
62. S. Lehner, K. Savage, M. Ciobanu, and D. E. Cliffel, Geochim. Cosmochim. Acta **71**, 2491 (2007).
63. S. Lehner and K. Savage, Geochim. Cosmochim. Acta **72**, 1788 (2008).
64. S. Mattila, J. A. Leiro, and K. Laajalehto, Appl. Surf. Sci. **212–213**, 97 (2003).
65. C. Jagadish and S. J. Pearton, *Zinc Oxide Bulk, Thin Films, and Nanostructures* (Elseviser, 2006).
66. B. D. Cullity, *Elements of X-Ray Diffraction,* 2nd edition (Addison-Wesley, Philippines, 1978), p 102.
67. J. A. Woollam Co., *Vertical VASE* (2007).
68. H. Fujiwara, *Spectroscopic Ellipsometry: Principles and Applications* (Wiley, 2007), p. 81.
69. D. R. Penn, Phys. Rev. **128**, 2093 (1962).
70. T. Yamada, T. Ueda, and T. Kitayama, J. Appl. Phys. **53**, 4328 (1982).
71. D. Banjara, Y. Malozovsky, L. Franklin, and D. Bagayoko, AIP Adv. **8,** 025212 (2018).
72. S. W. Lehner, K. S. Savage, and J. C. Ayers, J. Cryst. Growth **286**, 306 (2006).
73. E. Bastola, K. P. Bhandari, and R. J. Ellingson, J. Mater. Chem. C **5**, 4996 (2017).
74. P. Lazić, R. Armiento, F. W. Herbert, R. Chakraborty, R. Sun, M. K. Y. Chan, K. Hartman, T. Buonassisi, B. Yildiz, and G. Ceder, J. Phys. Condens. Matter **25**, 465801-1 (2013).
75. J. Tauc and A. Menth, Non Cryst. Solids **569**, 8 (1972).
76. R. Chandler and R. Bene, Phys. Rev. B: Solid State **8**, 4979 (1973).
77. I. Ferrer, F. Caballero, C. De las Heras, and C. Sánchez, Solid State Commun. **89**, 349 (1994).
78. R. Sun and G. Ceder, Phys. Rev. B: Condens. Matter Mater. Phys. **84**, 245211 (2011).
79. M. Kamruzzaman and J. A. Zapien, J. Nanosci. Nanotechnol. **17**, 5061 (2017).
80. A. M. A. E. Halim, S. Fiechter, and H. Tributsch, Electrochim. Acta **47**, 2615 (2002).